

Adhesion of Nonmotile *Pseudomonas aeruginosa* on “Soft” Polyelectrolyte Layer in a Radial Stagnation Point Flow System: Measurements and Model Predictions

Alexis J. de Kerchove,[†] Paweł Weroński,^{‡,§} and Menachem Elimelech^{*,†}

Department of Chemical Engineering, Environmental Engineering Program, Yale University, P.O. Box 208286, New Haven, Connecticut 06520-8286, Theoretical Division, Los Alamos National Laboratory, Mail Stop: B284, Los Alamos, New Mexico 87545, and Institute of Catalysis and Surface Chemistry, Polish Academy of Sciences, ul. Niezapominajek 8, 30-239 Kraków, Poland

Received June 28, 2007. In Final Form: August 5, 2007

Prediction of bacterial deposition rates onto substrates in natural aquatic systems is quite challenging because of the inherent complexity of such systems. In this study, we compare experimental deposition kinetics of nonmotile bacteria (*Pseudomonas aeruginosa*) on an alginate-coated substrate in a radial stagnation point flow (RSPF) system to predictions based on DLVO theory. The “softness” of the surface layer of the bacteria and alginate-coated substrate was considered in the calculations of their electrokinetic surface properties, and the relevance of both the classical zeta potential and the outer surface potential as surrogates for surface potential was investigated. Independent of the used electrical potentials, we showed that significant discrepancies exist between theory and experiments. Analysis of microscopic images in the RSPF system has demonstrated, for the first time, that irreversible deposition of particles or cells entrapped in the secondary energy minimum can occur on the alginate layer, despite the hydrodynamic forces resulting from the radial flow in the RSPF system. It is suggested that polymeric structures associated with the surface of the particle/cell and the alginate-coated substrate are responsible for the transition between the secondary minimum and primary energy well. This mode of deposition is likely to be important in the deposition of microorganisms in complex aquatic systems.

1. Introduction

The ability to control bacterial transport and deposition is of paramount importance in aquatic systems, including those in environmental and biomedical settings and industrial processes. Deposition of bacteria in engineered systems, such as membranes¹ or catheters,² results in the formation of biofilms, which significantly reduce the efficiency of such systems. Because standard mechanical cleaning procedures for the fouled system are often damaging, prevention of the initial bacterial adhesion remains the optimal control strategy. In contaminated groundwaters, microbial transport is the primary mechanism for the spread of pathogens³ and has been linked to widespread contamination in drinking and recreational waters. A better understanding and control of bacterial adhesion mechanisms could allow for the reduction of pathogen contamination. However, the control of microbial deposition is limited by the persisting disagreement between theoretical predictions and experimental measurements of deposition kinetics and the ubiquitous complexity of aquatic systems, which is usually oversimplified in experimental setups.

The Derjaguin–Landau–Verwey–Overbeek (DLVO) theory is commonly used to describe deposition kinetics of colloidal particles.^{4,5} However, the marked disagreement between predicted

total interaction energy profiles and experimental measurements of adhesion forces^{6,7} makes predictions of deposition kinetics difficult.⁸ Some of these discrepancies evidently result from the inability of the DLVO theory to completely capture the ensemble of possible colloidal interactions between the particles and the substrate. Several modified versions of the theory, which include additional colloidal forces, such as hydration, hydrophobic, and Born forces, have been developed to improve model predictions.^{7,9} Despite improvement of these theories to describe deposition trends of particles onto substrates, marked discrepancies between theory and experiments still remain in reported studies.^{6,10,11} Several other factors, not currently accounted for in theoretical models, have been shown to significantly affect particle deposition,^{12,13} such as localized favorable interactions between the particle and substrate and particle deposition in secondary energy minima. Both of these effects depend on the presence of heterogeneities at the surface of the particles and substrate, which are particularly important in natural aquatic systems.

The presence of localized surface heterogeneities on bacterial cell surfaces is characteristic of all bacterial cells due to their

* Corresponding author. Phone: (203) 432–2789. Fax: (203) 432–2881. E-mail: menachem.elimelech@yale.edu.

[†] Yale University.

[‡] Los Alamos National Laboratory.

[§] Polish Academy of Sciences.

(1) Flemming, H. C. *Appl. Microbiol. Biotechnol.* **2002**, *59* (6), 629–640.
(2) Tenke, P.; Kovacs, B.; Jackel, M.; Nagy, E. *World J. Urol.* **2006**, *24* (1), 13–20.

(3) Tufenkji, N.; Ryan, J. N.; Elimelech, M. *Environ. Sci. Technol.* **2002**, *36* (21), 422A–428A.

(4) Poortinga, A. T.; Bos, R.; Norde, W.; Busscher, H. J. *Surf. Sci. Rep.* **2002**, *47* (1), 3–32.

(5) Elimelech, M.; Gregory, J.; Jia, X.; Williams, R. A. *Particle Deposition and Aggregation: Measurement, Modeling and Simulation*; Butterworth-Heinemann: London, 1995.

(6) Abu-Lail, N. I.; Camesano, T. A. *Biomacromolecules* **2003**, *4* (4), 1000–1012.

(7) Hermansson, M. *Colloid Surf. B: Biointerfaces* **1999**, *14* (1–4), 105–119.

(8) Tufenkji, N.; Elimelech, M. *Langmuir* **2004**, *20* (25), 10818–10828.

(9) Meinders, J. M.; vanderMei, H. C.; Busscher, H. J. *J. Colloid Interface Sci.* **1995**, *176* (2), 329–341.

(10) Azeredo, J.; Visser, J.; Oliveira, R. *Colloid Surf. B: Biointerfaces* **1999**, *14* (1–4), 141–148.

(11) Rijnaarts, H. H. M.; Norde, W.; Lyklema, J.; Zehnder, A. J. B. *Colloid Surf. B: Biointerfaces* **1999**, *14* (1–4), 179–195.

(12) Chen, J. Y.; Ko, C. H.; Bhattacharjee, S.; Elimelech, M. *Colloid Surf. A: Physicochem. Eng. Asp.* **2001**, *191* (1–2), 3–15.

(13) Kuznar, Z. A.; Elimelech, M. *Colloid Surf. A: Physicochem. Eng. Asp.* **2007**, *294* (1–3), 156–162.

highly dynamic response to environmental conditions. These heterogeneities involve variations in surface charge and biological function of the molecular appendages protruding from the outer membrane of the bacteria,^{14–16} such as pili, flagella, lipopolysaccharides, and membrane bound proteins. Interactions between these cell surface appendages and substrates are responsible for the well-described mechanism of cell deposition, involving initial reversible deposition followed by either detachment or irreversible attachment.⁹

The presence of dissolved organic matter, such as polysaccharides, peptides, humic substances, and nucleic acid fragments is common to all aquatic systems. These substances adsorb at the solid–liquid interface and form a layer commonly known as the conditioning film.¹⁷ Previous attempts to characterize the impact of conditioning films, using saliva medium, blood plasma, or seawater dissolved organic carbon as conditioning matter, led to inhibition or enhancement of cell deposition.^{18–20} This inconsistency with respect to the impact of the conditioning film on bacterial deposition was attributed to changes in hydrophobicity and roughness of the conditioned substrate. Relating the deposition behavior to the relevant surface interactions has not been possible due to the complexity of the conditioning film matrix used in experimental setups. Complex films of adsorbed macromolecules add surface heterogeneities to the substrate, which can be (i) physical (i.e., enhanced roughness and viscoelasticity of the film²¹), (ii) chemical (i.e., variability in charged functional groups), or (iii) biological (i.e., ligands binding to a specific receptor site at the cell surface²²). We have recently shown that an adsorbed alginate layer can be used as a model conditioning film.²³ A well-defined adsorbed layer of polysaccharides enhanced the deposition of motile and nonmotile bacteria, likely by increasing the structural and chemical surface heterogeneities at the substrate surface.²³

The aim of this paper is to model the initial deposition kinetics of bacteria onto a conditioning film. Specifically, we compare the initial deposition kinetics obtained from well-controlled bacterial deposition experiments to theoretical predictions based on DLVO theory. Experiments were conducted using a newly designed radial stagnation point flow system that allows high-resolution imaging of the deposition of cells by contrast phase microscopy. A nonflagellated, nonpiliated mutant of *Pseudomonas aeruginosa*, PAO1 Δ fliC Δ pilA, was used in order to reduce the degree of cell surface complexity and therefore facilitate the understanding and modeling of the role of the conditioning film. We demonstrated that use of either the outer surface potential or the zeta potential as surrogates for bacterial surface potential yields similar predictions of cell deposition kinetics onto bare or alginate-coated substrates. In all cases, theoretical predictions substantially underestimated the measured bacterial deposition

kinetics. We discuss the main reasons for discrepancies between theoretical predictions and experimental results by considering the complex structure of the bacterial and substrate surfaces.

2. Materials and Methods

2.1. Model Bacterial Strain and Substrates. The nonmotile *P. aeruginosa* strain, PAO1 Δ fliC Δ pilA, was used as a model bacterial cell. We have shown in our previous work that this strain, mutated by allelic exchange, is deficient in the biosynthesis of type IV pilus protein and flagellin and subsequently lacks twitching and swimming motilities.²³ PAO1 Δ fliC Δ pilA was shown to be viable and to have a constant cell size and shape over a wide range of ionic strengths. The average major and minor axes of the rod-shaped cells are $2.42 \pm 0.48 \mu\text{m}$ and $0.93 \pm 0.05 \mu\text{m}$, respectively, which are equivalent to a volumetric spherical diameter of $1.28 \mu\text{m}$.

The following protocol was applied to all liquid cell cultures used in the characterization or deposition kinetics experiments. PAO1 Δ fliC Δ pilA was incubated in LB at 37 °C and harvested at mid-exponential growth phase. The bacterial suspension was centrifuged (Sorvall RC-26 Plus) for 15 min at 1000g. The cell pellet was washed once with 100 mM KCl solution, recentrifuged under the same conditions, and finally resuspended in KCl (100 mM). We used a carboxylated modified latex (CML) particle ($1.2 \mu\text{m}$ in diameter) as a model nonbiological particle (Invitrogen, CA).

Ultrapure quartz coverslips measuring 25 mm in diameter and 0.1 mm thick (Electron Microscopy Sciences, PA) were used in the deposition experiments. Before use, the coverslips were cleaned in a three-step process: (i) 2% Hellmanex II bath (overnight, 75 °C) (Hellma GmbH & Co. KG, Germany), (ii) Nochromix bath (overnight, 25 °C) (Godax Laboratories, Inc., MD), and (iii) baking (1 to 3 h, 560 °C). Coverslips were thoroughly rinsed with DI water after steps (i) and (ii).

Favorable (nonrepulsive) deposition conditions between the particles and the substrate were obtained by chemically modifying the coverslip surface. Charge reversal was induced by adsorption of a layer of poly-L-lysine (PLL) at the quartz surface. PLL hydrobromide (Sigma, MO) has an average molecular weight of 110 kDa. The quartz coverslips were submerged in 0.1 g/L and 0.22 μm -filtered PLL/HEPES (pH 5.6) solution overnight at 4 °C and rinsed 4 times with 0.22 μm -filtered DI water. The quartz coverslips were dried for 3 h under vacuum at 37 °C. Particle deposition experiments under favorable conditions were performed over a wide range of ionic strengths (1 to 100 mM) at ambient pH (pH 5.4–5.6).

Alginate conditioning films were formed by adsorption of alginate (0.1 g/L, 10 mM KCl solution) for 15 min on PLL-coated quartz under laminar flow conditions. We used commercial sodium alginate (Sigma, MO) with an average molecular weight of 72.7 kDa. The alginate films were rinsed for 15 min with the electrolyte solution of interest prior to conducting the bacterial deposition experiment in the radial stagnation point flow system.²⁴

2.2. Calculation of Surface Potentials. Extensive characterization of the electrokinetic properties of the bacterial cells and substrates was presented in our previous work.²³ Bare and alginate-coated silica particles measuring $1.6 \mu\text{m}$ in diameter (Bangs Laboratories, Inc., IN) were used as surrogates for the clean and surface-modified quartz slides.²³ Measurements of the electrophoretic mobility (ZetaPALS, Brookhaven Instruments Corp., NY) of CML particles as a function of ionic strength were obtained according to procedures previously described in de Kerchove and Elimelech.²⁵ All electrophoretic mobilities were converted to zeta potentials (ζ) using the Smoluchowski equation. This equation is applicable because of the relatively large size of the particles and the ionic strengths used.⁵

The outer surface potentials (OSP) of the bacterial cells, CML particles, and substrates were calculated from the measured electrophoretic mobilities using Ohshima's theory for soft particles.²⁶ In this theory, the ion-penetrable layer of polyelectrolytes at the

(14) Walker, S. L.; Redman, J. A.; Elimelech, M. *Langmuir* **2004**, *20* (18), 7736–7746.

(15) Klausen, M.; Heydorn, A.; Ragas, P.; Lambertsen, L.; Aaes-Jorgensen, A.; Molin, S.; Tolker-Nielsen, T. *Mol. Microbiol.* **2003**, *48* (6), 1511–1524.

(16) Ishii, S. I.; Unno, H.; Miyata, S.; Hori, K. *Biosci. Biotechnol. Biochem.* **2006**, *70* (11), 2635–2640.

(17) Costerton, J. W.; Lewandowski, Z.; Caldwell, D. E.; Korber, D. R.; Lappinscott, H. M. *Annu. Rev. Microbiol.* **1995**, *49*, 711–745.

(18) Bakker, D. P.; Klijnsma, J. W.; Busscher, H. J.; van der Mei, H. C. *Biofouling* **2003**, *19* (6), 391–397.

(19) Jones, D. S.; McGovern, J. G.; Adair, C. G.; Woolfson, A. D.; Gorman, S. P. *J. Mater. Sci.-Mater. Med.* **2001**, *12* (5), 399–405.

(20) Linton, C. J.; Sheriff, A.; Millar, M. R. *J. Appl. Microbiol.* **1999**, *86* (2), 194–202.

(21) Dufre ne, Y. F.; Marchal, T. G.; Rouxhet, P. G. *Langmuir* **1999**, *15* (8), 2871–2878.

(22) van Hoogmoed, C. G.; van der Kuijl-Booij, M.; van der Mei, H. C.; Busscher, H. J. *Appl. Environ. Microbiol.* **2000**, *66* (2), 659–663.

(23) de Kerchove, A. J.; Elimelech, M. *Appl. Environ. Microbiol.* **2007**, *73*, 5227–5234.

(24) de Kerchove, A. J.; Elimelech, M. *Macromolecules* **2006**, *39* (19), 6558–6564.

(25) de Kerchove, A. J.; Elimelech, M. *Langmuir* **2005**, *21* (14), 6462–6472.

(26) Ohshima, H. *J. Colloid Interface Sci.* **1994**, *163* (2), 474–483.

surface of the particles is characterized by two parameters: the fixed charge density, ρ_{fix} , and the electrophoretic softness, $1/\lambda$.²⁶ Details on the application of Ohshima's theory to measured electrophoretic mobilities of particles and bacterial cells can be found in our previous work.²⁵

2.3. Radial Stagnation Point Flow System. Bacterial deposition rates were studied in a newly designed radial stagnation point flow system (RSPF) that allows high-resolution imaging of the deposition of cells by contrast phase microscopy. Details on the setup of the RSPF system can be found in our recent work.²³ Deposition was recorded in a rectangular viewing area of $220 \mu\text{m} \times 165 \mu\text{m}$ (captured in a $140 \mu\text{m}$ radius circle) at regular intervals (10 to 20 s) for 10 min with a DP70 digital camera (Olympus).

The hydrodynamics of the RSPF system are well-defined²⁷ and were confirmed for the specific dimensions of our flow cell by solving the stationary Navier–Stokes equation for laminar flow in the vicinity of the stagnation point (FEMLAB, COMSOL). No slip conditions were assumed on all internal walls of the RSPF cell. Our RSPF system is characterized by an injection capillary radius R of 1 mm and a distance h between the capillary outlet and the collector surface of 2 mm. During experiments, a constant flow of 4.93 mL/min (average capillary velocity = 2.65 cm/s) was induced by a syringe pump (KD Scientific Inc., New Hope, PA). The Reynolds number at the outlet of the capillary is 28.4.⁵ All experiments were carried out under the same hydrodynamic conditions and at 25 °C (± 1 °C).

2.4. Deposition Kinetics Protocol. Bacterial cell deposition was studied as a function of ionic strength in monovalent (KCl) salt at ambient pH (pH 5.4–5.6). Electrolyte solutions were prepared with DI water and reagent grade salt (Fisher Scientific) and stored at 4 °C. For each cell culture, the cell concentration was determined in a Buerker-Tuerk cytometer chamber (Marienfeld Laboratory Glassware, Germany). Prior to each experiment, concentrated cell suspensions were diluted into the electrolyte solution of interest.

For each bacterial deposition experiment, the bacterial transfer rate coefficient, k_{RSPF} , was calculated as the ratio between the bacterial deposition flux and the initial bacterial bulk concentration.¹⁴ The bacterial deposition flux is the observed deposition rate of bacteria normalized by the camera viewing area. Bacterial deposition kinetics are represented as attachment (sticking) efficiency, α .²⁸ The attachment efficiency corresponds to the bacterial transfer rate coefficient normalized by the bacterial transfer rate coefficient measured under favorable (nonrepulsive) conditions (i.e., on PLL-coated quartz). Reported values of attachment efficiency are averages of data taken from 2–4 experiments conducted using discrete cell cultures.

2.5. Prediction of Cell Deposition using DLVO Theory. We have calculated the cell/particle deposition rate in the RSPF system by numerically solving the convective-diffusion equation with colloidal and hydrodynamic interactions fully incorporated.⁵ Briefly, the starting point is the convective-diffusion equation:

$$\nabla \cdot (\mathbf{u}C) = \nabla \cdot (\mathbf{D} \cdot \nabla C) - \nabla \cdot \left(\frac{\mathbf{D} \cdot \mathbf{F}}{kT} C \right) \quad (1)$$

where C is the particle concentration, \mathbf{D} is the particle diffusion tensor, \mathbf{u} is the particle velocity induced by the flow of the suspending medium, T is the absolute temperature, and \mathbf{F} is the external force vector. The latter is the sum of the net gravity and buoyancy \mathbf{F}_G , and colloidal, \mathbf{F}_{col} , forces:

$$\mathbf{F} = \mathbf{F}_G + \mathbf{F}_{\text{col}} \quad (2)$$

The colloidal force is derived from the total interaction potential, ϕ_T , as follows:

$$\mathbf{F}_{\text{col}} = -\nabla \phi_T \quad (3)$$

Considering the DLVO theory, the total interaction potential is the sum of the electrostatic double layer and van der Waals interactions taking place between the particles and the collector surface. Electrostatic double layer interaction energies were calculated using the constant surface potential expression of Hogg et al. for a sphere–plate system.²⁹ The surface potentials were replaced by either the zeta potentials or the outer surface potentials of the particles and substrates. The expression for retarded van der Waals interaction proposed by Gregory³⁰ was used to calculate the attractive interaction energy. To calculate the van der Waals interaction energies, we used a Hamaker constant of 6.5×10^{-21} J for the bacterial cell–water–quartz system,^{14,31–33} and of 1×10^{-20} J for the latex–water–quartz system.^{34,35}

The convective-diffusion equation (eq 1) is a second order, linear, ordinary differential equation that can only be solved numerically. Numerical integration of this equation is not trivial because of the coupling between the bulk transport (macroscale) and the transport through the thin boundary layer (microscale), where the rapidly changing, strong surface interactions have to be taken into account. This is especially the case when an energy barrier and secondary minimum exist in the system. To solve this stiff differential equation, we employed the method described by Weroński and Elimelech.³⁶ After solving numerically for the concentration distribution of particles in the region of the stagnation point flow, the particle deposition flux and the corresponding particle transfer rate coefficients were calculated as described elsewhere.⁵

3. Results and Discussion

3.1. Flow Field in the Stagnation Point. The study of mass (or particle) transfer in the RSPF system is facilitated by the uniform hydrodynamic and diffusion boundary layers in the vicinity of the stagnation point. The resulting one-dimensional deposition at the collector surface depends on the transport of particles in the boundary layer at the stagnation point flow region, which is often characterized by the Peclet number. This parameter represents the strength of the fluid flow (convection) relative to Brownian motion (diffusion):²⁷

$$Pe = \frac{\alpha_s a_p^3}{D_0} \quad (4)$$

Here, D_0 is the diffusion coefficient of a particle of radius a_p and α_s is a flow intensity parameter characterizing the flow field.

The flow intensity parameter depends on the Reynolds number, Re , and the geometry of the system, which is defined by the ratio h/R , where h is the distance between the capillary outlet and the collector surface and R is the radius of the inlet capillary.²⁷ A dimensionless form of this parameter can be used to characterize the flow field of the RSPF system²⁷

$$\alpha_s^* = \frac{\alpha_s R^3 \rho}{Re \mu} \quad (5)$$

(29) Hogg, R.; Healy, T. W.; Fuersten, Dw. *Trans. Faraday Soc.* **1966**, *62* (522P), 1638–1651.

(30) Gregory, J. J. *Colloid Interface Sci.* **1981**, *83* (1), 138–145.

(31) Redman, J. A.; Walker, S. L.; Elimelech, M. *Environ. Sci. Technol.* **2004**, *38* (6), 1777–1785.

(32) Truesdail, S. E.; Lukasik, J.; Farrah, S. R.; Shah, D. O.; Dickinson, R. B. *J. Colloid Interface Sci.* **1998**, *203* (2), 369–378.

(33) Simoni, S. F.; Bosma, T. N. P.; Harms, H.; Zehnder, A. J. B. *Environ. Sci. Technol.* **2000**, *34* (6), 1011–1017.

(34) Elimelech, M.; O'Melia, C. R. *Environ. Sci. Technol.* **1990**, *24* (10), 1528–1536.

(35) Elimelech, M. *J. Colloid Interface Sci.* **1994**, *164* (1), 190–199.

(36) Weroński, P.; Elimelech, M. *J. Colloid Interface Sci.* submitted.

(27) Dabros, T.; van de Ven, T. G. M. *Colloid Polym. Sci.* **1983**, *261* (8), 694–707.

(28) Elimelech, M. *Water Res.* **1992**, *26* (1), 1–8.

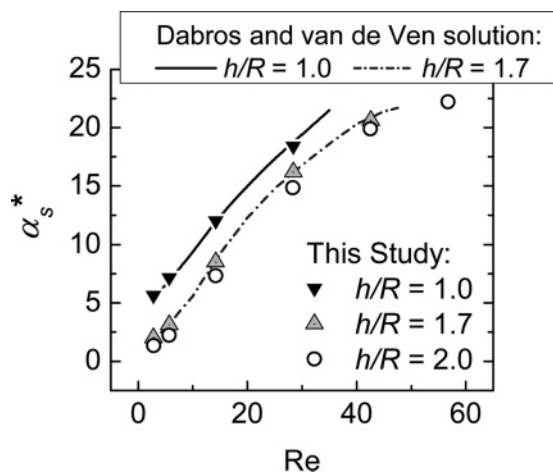


Figure 1. Verification of the dependence of the dimensionless flow intensity parameter, α_s^* , on the Reynolds number. Our numerical solutions of the flow intensity parameter for h/R of 1.0 and 1.7 (triangles) are compared to the numerical solutions of the flow intensity parameter for similar h/R values obtained by Dabros and van de Ven²⁷ (solid and dashed lines, respectively). The open circles are the values of the flow intensity parameter corresponding to the RSPF geometry used in this study ($h/R = 2.0$).

where ρ and μ are the density and absolute viscosity of the fluid, respectively.

In order to calculate the parameter α_s^* of our RSPF system, we solved numerically the Navier–Stokes equation for laminar flow in the vicinity of the stagnation point. At this point, the flow field can be described in terms of the spatial coordinates r and z of the cylindrical coordinate system

$$v_r = \alpha_s r z \quad (6)$$

$$v_z = -\alpha_s z^2 \quad (7)$$

where v_r and v_z are the radial and axial velocity components of the fluid. To verify the validity of our numerical solution, we studied the dependence of α_s^* as a function of the Reynolds number and compared it to the solution published by Dabros and van de Ven²⁷ (Figure 1). We successfully reproduced the values of α_s^* that were obtained for two systems with h/R of 1.0 and 1.7. We then proceeded to predict the variation of α_s^* for our RSPF system ($h/R = 2.0$) as a function of the Reynolds number and calculated an α_s^* of 14.85 for the Reynolds number used in our deposition experiments ($Re = 28.4$; Figure 1). This value of the dimensionless flow intensity parameter is close to the value of 16.53 that was obtained using the following approximation, which is appropriate to the geometry of our system:³⁷

$$\alpha_s^*(Re) = \frac{0.0734Re^2 + 0.8}{0.01735Re^{3/2} + 1} \quad (8)$$

The above hydrodynamic characteristics of the RSPF system hold for an area where the stagnation point flow conditions exist. The radial extension of this region was defined by Dabros and van de Ven²⁷ as the distance where the wall vorticity ω_s changes within 3 to 4% of its value at $r = 0$. Such variations have been shown to have only a small influence on the mass transfer calculations.²⁷ Based on our numerical solution of the flow field, we calculated the wall vorticity of our system and defined the boundaries of the stagnation point region. For a Reynolds number



Figure 2. Experimental electrophoretic mobility of (A) CML particles and (B) nonmotile PAO1 $\Delta fliC \Delta pilA$ bacteria, and corresponding electrical surface potentials, as a function of ionic strength (KCl). Electrophoretic mobility data were (i) converted to zeta potential using the Smoluchowski equation (symbols) and (ii) fitted with Ohshima's electrokinetic theory for "soft" particles (solid line).²⁶ Ohshima's outer surface potential was then calculated (dashed line). Experiments were carried out at an ambient pH (5.5–5.7) and a temperature of 25 °C (± 1 °C).

of 28.4, we calculated a 3% change in wall vorticity at a radius r of 180 μm , which is 30% larger than that of the circular viewing area considered in our deposition experiments ($r = 140 \mu\text{m}$). This confirms that the geometry of our RSPF system and the viewing area capture the deposition phenomena in the well-defined stagnation point flow field.

3.2. Characterization of Surface Potentials. Electrophoretic mobilities as a function of ionic strength for bacterial cells and CML particles (Figure 2), as well as the bare and alginate-coated substrates (Figure 3), were converted to zeta potentials using the Smoluchowski equation and to outer surface potentials using Ohshima's equation for soft particles.²⁶ The measured electrophoretic mobilities demonstrated the effect of ionic strength on the screening of surface charge and compression of the electrical double layer. However, complete screening of the surface charge at high ionic strength was achieved only for the bare quartz substrate where the surface potential vanishes (Figure 3A). The significant residual electrophoretic mobility at high ionic strength for CML particles (Figure 2A), bacterial cells (Figure 2B), and alginate-coated silica particles (Figure 3B) is characteristic of these "soft" surfaces having an ion-permeable polyelectrolyte layer at the surface.²⁶

The best fits by Ohshima's equation were obtained for electrophoretic mobility data collected at ionic strengths above 10–50 mM as previously suggested (Figure 2 and 3)³⁸ and allowed for the calculation of the fixed charge density and electrophoretic softness of the surface layer for each particle type (Table 1). A significantly poorer fit of electrophoretic mobility data was

(37) Warszynski, P. *Adv. Colloid Interface Sci.* **2000**, *84* (1–3), 47–142.

(38) Sonohara, R.; Muramatsu, N.; Ohshima, H.; Kondo, T. *Biophys. Chem.* **1995**, *55* (3), 273–277.

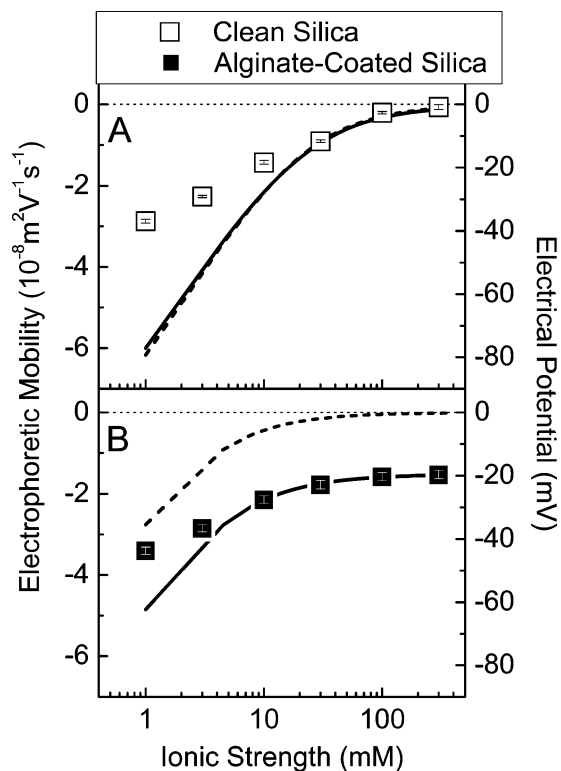


Figure 3. Experimental electrophoretic mobility of (A) pure and (B) alginate-coated quartz (represented by silica particles) and corresponding electrical surface potentials as a function of ionic strength (KCl). Electrophoretic mobility data were (i) converted to zeta potentials using the Smoluchowski equation (symbols) and (ii) fitted with Ohshima's electrokinetic theory for "soft" particles (solid line).²⁶ Ohshima's outer surface potential was then calculated (dashed line). Experiments were carried out at an ambient pH (5.5–5.7) and a temperature of 25 °C (± 1 °C).

Table 1. Calculated Values of the Fixed Charge Density (ρ_{fix}) and Electrophoretic Softness ($1/\lambda$) for the Bacterial Cells, CML Particles, and Clean and Alginate-Coated Silica Particles Obtained by Fitting Electrophoretic Mobility Data Using Ohshima's Theory for Soft Particles,²⁶ ρ_{fix} , and the Electrophoretic Softness, $1/\lambda$

particle/cell type	fixed charge density (mM)	electrophoretic softness (nm)
PAO1 Δ <i>fliC</i> Δ <i>pilA</i>	−95	0.85
CML particles	−167	0.95
clean SiO ₂	−59	0.14
alginate-coated SiO ₂	−9	4.11

observed at low ionic strength for bacteria and bare silica when compared to CML and coated silica. Such deviation from theoretical predictions of electrophoretic mobility can be attributed to either the high degree of heterogeneity in the charge and resistance to flow of the soft polymer layer for the bacteria³⁸ or to the absence of an ion-permeable layer at the surface of the hard bare silica particles.³⁹ However, the subsequent conditioning of the silica particle surface with alginate increased their electrophoretic softness 29-fold and reduced the fixed charge density by 7-fold (Table 1). These differences in softness and charge density between bare and alginate-conditioned silica particles reflect the successful formation of a "soft" polyelectrolyte layer at their surface during conditioning.

For each particle type, the outer surface potential and zeta potential were calculated and compared (Figures 2 and 3). For

hard spheres such as bare silica particles (Figure 3A), the outer surface potential was equal to the zeta potential of the particles. However, in the presence of an ion-permeable layer at the surface of the particles, such as for bacteria, CML, and alginate-coated silica, the outer surface potential was much smaller than the zeta potential and tended to a zero value at high ionic strength (Figures 2 and 3B). The outer surface potential represents only the surface charges that are exposed to the surrounding electrolyte solution and can therefore be effectively shielded by counterions until complete screening at high salt concentrations is achieved.²⁶

3.3. DLVO Interaction Energy Predictions. In order to explain the deposition kinetics of bacterial cells and CML particles at the stagnation point, we resort to DLVO interaction energy calculations. Repulsive electrostatic interactions were calculated by using either zeta potentials or outer surface potentials as surrogates for the surface potentials of the particles/cells and the substrate. The retarded van der Waals contribution to the sphere–plate interaction energy was determined using Hamaker constants of 1×10^{-20} and 6.5×10^{-21} J for the latex–water–quartz^{28,35} and bacteria–water–quartz systems,^{14,31–33} respectively.

Considering the outer surface potential as the surface potential in the DLVO calculations suggests the use of different separation distances for electrostatic and van der Waals interactions as discussed in our previous work.²⁵ We have previously shown that accounting for a thickness of only a few nanometers for the polyelectrolyte layer at the particle or substrate surface, as a difference in separation distance between van der Waals and electrostatic forces, can result in major differences in predictions of total interaction energy. However, this distinction in separation distances is not commonly made in other similar studies using the outer surface potential to predict bacterial deposition.^{4,40–42} Because the thicknesses of the ion-permeable layers at the surface of the particle and substrate are not exactly known, we used the same separation distance for both interaction forces and defined it as the distance between the surfaces of the inner core materials of both the particle and the substrate.

Calculated DLVO interaction energy profiles are characterized by three features that can help to explain the deposition behavior: (i) the repulsive energy barrier, (ii) the depth of the secondary energy minimum, and (iii) the distance of the secondary minimum from the substrate. We calculated the dependence of these three DLVO features on ionic strength for systems where particles (cells) are interacting with either clean or alginate-coated quartz surfaces.

3.3.1. Bare Quartz Substrate. The total interaction energy profiles between particles (cells) and bare quartz (Table 2) indicated that energy barriers were suppressed at an ionic strength above 100 mM. This ionic strength defines the transition between repulsive (unfavorable) and nonrepulsive (favorable) conditions for deposition. Under unfavorable conditions (i.e., ionic strengths ranging from 3 to 30 mM), substantial energy barriers were predicted for CML particles and bacterial cells. At low ionic strength (3 mM), a large difference between the energy barriers calculated with either zeta or outer surface potentials was observed and was attributed to the poor fitting of Ohshima's theory to electrophoretic mobility data. At that ionic strength, the theory predicted an erroneously strong outer surface potential for the particles, which resulted in an energy barrier much larger than that calculated using zeta potentials. Total interaction energy

(40) Abu-Lail, N. I.; Camesano, T. A. *Environ. Sci. Technol.* **2003**, *37* (10), 2173–2183.

(41) Morisaki, H.; Nagai, S.; Ohshima, H.; Ikemoto, E.; Kogure, K. *Microbiol. (UK)* **1999**, *145*, 2797–2802.

(42) Hayashi, H.; Tsuneda, S.; Hirata, A.; Sasaki, H. *Colloid Surf. B: Biointerfaces* **2001**, *22* (2), 149–157.

(39) Tschapek, M.; Santamar, R.; Natale, I. *Electrochim. Acta.* **1969**, *14* (9), 889–895.

Table 2. Energy Barrier, Secondary Minimum Depth, and Distance of the Secondary Energy Minimum from the Surface between Clean (Bare) Quartz Substrate and Either (A) CML Particles or (B) PAO1 Δ fl*c* Δ pil*A* Cells as a Function of Ionic Strength (KCl)^a

A – CML particles						
ionic strength (mM)	zeta potential			outer surface potential		
	energy barrier (kT)	secondary minimum depth (kT)	distance of secondary energy minimum (nm)	energy barrier (kT)	secondary minimum depth (kT)	distance of secondary energy minimum (nm)
3	965.7	-0.37	58.3	1873.5	-0.35	60.1
10	334.9	-1.74	24.5	507.4	-1.77	24.3
30	63.9	-7.58	9.7	14.7	-10.02	7.6
100	NB ^b	NB ^b	NB ^b	NB ^b	NB ^b	NB ^b
300	NB ^b	NB ^b	NB ^b	NB ^b	NB ^b	NB ^b

B – PAO1 Δ fl <i>c</i> Δ pil <i>A</i> cells						
ionic strength (mM)	zeta potential			outer surface potential		
	energy barrier (kT)	secondary minimum depth (kT)	distance of secondary energy minimum (nm)	energy barrier (kT)	secondary minimum depth (kT)	distance of secondary energy minimum (nm)
3	574.5	-0.29	53.9	1784.4	-0.23	61.7
10	217.3	-1.39	22.3	560.7	-1.12	25.8
30	27.5	-6.30	8.3	15.4	-6.85	7.7
100	NB ^b	NB ^b	NB ^b	NB ^b	NB ^b	NB ^b
300	NB ^b	NB ^b	NB ^b	NB ^b	NB ^b	NB ^b

^a Surface potentials of particles (cells) and collectors were replaced by either measured mean zeta potentials or calculated outer surface potentials. Hamaker constants were 1×10^{-20} and 6.5×10^{-21} J for the latex–water–quartz²⁸ and bacteria–water–quartz^{14,31–33} interacting media, respectively. The equivalent spherical diameter and the density of both the particles and the cells were $1.2 \mu\text{m}$ and 1.055 g/cm^3 , respectively. Other experimental conditions employed were a capillary Reynolds number of 28.4, a particle (or cell) Peclet number of 0.22, an ambient pH (5.5–5.7), and a temperature of $25 \text{ }^\circ\text{C}$ ($\pm 1 \text{ }^\circ\text{C}$). ^b No barrier to deposition and hence no secondary minimum.

Table 3. Energy Barrier, Secondary Minimum Depth, and Distance of the Secondary Energy Minimum from the Surface between Alginate-Coated Quartz Substrate and Either (A) CML Particles or (B) PAO1 Δ fl*c* Δ pil*A* Cells as a Function of Ionic Strength (KCl)^a

A – CML particles						
ionic strength (mM)	zeta potential			outer surface potential		
	energy barrier (kT)	secondary minimum depth (kT)	distance of secondary energy minimum (nm)	energy barrier (kT)	secondary minimum depth (kT)	distance of secondary energy minimum (nm)
3	1480.9	-0.36	60	152.3	-0.48	49.8
10	755.4	-1.56	26.3	4.5	-3.24	15.7
30	365.7	-5.94	11.7	NB ^b	NB ^b	NB ^b
100	48.4	-25.23	4.1	NB ^b	NB ^b	NB ^b
300	NB ^b	NB ^b	NB ^b	NB ^b	NB ^b	NB ^b

B – PAO1 Δ fl <i>c</i> Δ pil <i>A</i> cells						
ionic strength (mM)	zeta potential			outer surface potential		
	energy barrier (kT)	secondary minimum depth (kT)	distance of secondary energy minimum (nm)	energy barrier (kT)	secondary minimum depth (kT)	distance of secondary energy minimum (nm)
3	734.90	-0.28	55.7	164.5	-0.32	51.5
10	405.90	-1.23	24.2	11.7	-1.93	17.7
30	163.60	-4.76	10.5	NB ^b	NB ^b	NB ^b
100	7.80	-18.26	3.9	NB ^b	NB ^b	NB ^b
300	NB ^b	NB ^b	NB ^b	NB ^b	NB ^b	NB ^b

^a Surface potentials of particles (cells) and collectors were replaced by either measured mean zeta potentials or calculated outer surface potentials. Hamaker constants were 1×10^{-20} and 6.5×10^{-21} J for the latex–water–quartz²⁸ and bacteria–water–quartz^{14,31–33} interacting media, respectively. The equivalent spherical diameter and the density for both the particles and the cells were $1.2 \mu\text{m}$ and 1.055 g/cm^3 , respectively. Other experimental conditions employed were a capillary Reynolds number of 28.4, a particle (cell) Peclet number of 0.22, an ambient pH (5.5–5.7), and a temperature of $25 \text{ }^\circ\text{C}$ ($\pm 1 \text{ }^\circ\text{C}$). ^b No barrier to deposition and hence no secondary minimum.

predictions also indicated the presence of secondary energy minima of statistically equivalent depths for CML particles and bacterial cells (Table 2). The depth of these energy wells increased with increasing ionic strength and reached a maximum value ranging between -6.30 and -10.02 kT at 30 mM ionic strength. As the depth of the energy wells increased, their distance from the substrate decreased to a minimum value ranging between 7.6 and 9.7 nm at 30 mM ionic strength.

3.3.2. Alginate-Coated Substrate. Total interaction energy profiles between particles (cells) and alginate coated substrates (Table 3) predicted very different ranges of unfavorable conditions, according to the potential used as the surface potential surrogate. The ionic strengths at which the calculated energy barriers vanish were above 100 and 10 mM when using, in calculations, the zeta potential and the outer surface potential, respectively.

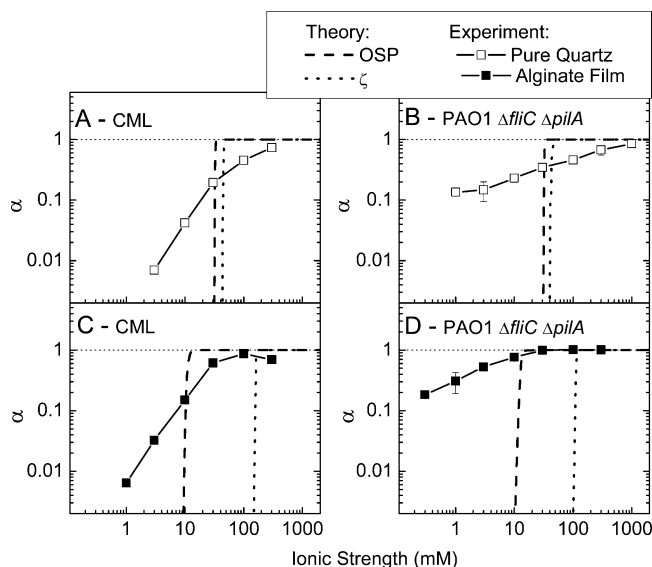


Figure 4. Comparison of theoretical and experimental attachment efficiency curves of CML particles and nonmotile PAO1 $\Delta fliC \Delta pilA$ bacteria on pure (A and B) and alginate-coated quartz (C and D), respectively, as a function of ionic strength (KCl). The deposition kinetics are expressed as the attachment efficiency, α . Surface potentials of particles and collectors were replaced by either calculated outer surface potentials (OSP), or the measured mean zeta potentials (ζ). The capillary flow rate in the RSPF system was fixed at 4.93 mL/min (average velocity of 26.5 cm/s), resulting in a capillary Reynolds number of 28.4 and a particle (cell) Peclet number of 0.22. Other experimental conditions employed were an ambient pH (5.5–5.7) and a temperature of 25 °C (± 1 °C). Error bars indicate one standard deviation.

Unfavorable conditions for particle (cell) deposition obtained when using zeta potentials were characterized by deep secondary minima that reached values of -25.23 and -18.26 kT for CML particles and bacterial cells, respectively, at an ionic strength of 100 mM. Correspondingly, the distances of the secondary minimum from the substrate reached values of 4.1 and 3.9 nm for CML particles and bacterial cells, respectively. These depths and distances of the energy wells were significantly deeper and shorter, respectively, than those calculated using lower ionic strengths. In contrast, when the outer surface potentials were used, secondary energy minima were practically nonexistent at most ionic strengths, with a maximum depth and minimum distance of -3.24 kT and 15.7 nm for CML particles, and -1.93 kT and 17.7 nm for bacterial cells.

3.4. Comparison of Experimental Deposition Kinetics to DLVO Predictions. In order to determine the relevance of DLVO energy profiles in predicting bacterial deposition, we compared theoretical deposition kinetics based on DLVO calculations to experimental attachment efficiencies measured in the RSPF system. Predicted deposition kinetics were in marked contrast to experimental results for both CML particles and bacteria depositing onto either clean or coated quartz (Figure 4). The major discrepancies between theory and experiments were found in the slope of the attachment efficiency curves under unfavorable conditions and in the value of the critical deposition concentration (CDC).

In all situations, experimental and theoretical attachment efficiencies increased with increasing ionic strength until the CDC value was reached, after which attachment efficiency stayed constant (Figure 4). However, the slopes of the theoretical deposition curves were much larger than those of the observed deposition kinetics curves, indicating significant underestimation of the deposition kinetics of particles (and cells) on bare and

conditioned substrates. This discrepancy was common to all of our theoretical curves, as found in other theoretical particle deposition studies.^{5,28,43} The discrepancy between theory and experiment appeared greater for bacterial cells than for CML particles as evidenced by the much steeper slopes observed in experiments with the CML particles, compared to those with bacterial cells.

The magnitude of the CDC is the only characteristic of the theoretical attachment efficiency curves that allows for the assessment of the impact of use of either zeta or outer surface potentials on deposition predictions. On clean quartz (Figure 4, panels A and B), theoretical attachment efficiency curves for the CML particles and bacteria predicted similar CDC values for both electrical potentials, which averaged about 50 and 35 mM when zeta potentials and outer surface potentials were used, respectively. These theoretical predictions of the CDC were an order of magnitude lower than those obtained experimentally for both particle types. On alginate-coated quartz (Figure 4, panels C and D), the CDC values predicted using outer surface potentials, which were 1 order of magnitude smaller than those calculated using zeta potentials, were equivalent to the CDCs of our experimental attachment efficiency curves that ranged between 10 and 30 mM. These results suggest that on conditioned substrates, the use of the outer surface potential allows for a good prediction of the ionic conditions required for the deposition of particles in a primary energy well, namely conditions favorable for deposition.

3.5. Role of the Secondary Energy Minimum. The entrapment of particles in secondary energy minima is theoretically possible when the sum of the particle thermal energy and the fluid drag force is small enough to maintain the particle in the energy well.⁴⁴ Substantial experimental evidence demonstrated that secondary energy minimum entrapment is important in the transport and deposition of particles in porous media.^{13,31} It was further shown that consideration of secondary minimum deposition significantly improves the agreement between theory and experimental data of deposition in porous media.^{31,45,46} However, in RSPF systems, it was suggested that because of the unique hydrodynamic flow conditions, particles trapped in the secondary energy minimum are swept away from the stagnation point center by the radial component of the flow parallel to the substrate.³¹

3.5.1. CML Particles. Direct microscopic observation of deposition of CML particles trapped in the secondary minimum onto an alginate-coated quartz substrate is shown in Figure 5. This observation suggests that this deposition mode could be responsible for a fraction of the observed deposited particles in our RSPF system. The superposition of nine successive pictures taken over a time of ca. 3 s allowed for the detection of slowly moving particles that were located in the vicinity of the substrate surface. In this image, moving particles appeared as paths of nine aligned points, whereas stagnant particles adhering to the substrate appeared as single darker points. We verified the trajectory and distance of moving particles trapped in secondary energy minima by fitting a linear line across the nine aligned points. The convergence of these lines at the center of the picture (circle, Figure 5A) determined the exact location of the stagnation point flow. By capturing these images at specific time intervals (15 s), we differentiated the particles trapped in secondary wells from those which deposited irreversibly. Depositing particles

(43) Gregory, J.; Wishart, A. J. *Colloids Surf.* **1980**, *1* (3–4), 313–334.

(44) Hahn, M. W.; Abadzic, D.; O'Melia, C. R. *Environ. Sci. Technol.* **2004**, *38* (22), 5915–5924.

(45) O'Melia, C. R.; Hahn, M. W.; Chen, C. T. *Water Sci. Technol.* **1997**, *36* (4), 119–126.

(46) Tufenkji, N.; Elimelech, M. *Langmuir* **2005**, *21* (3), 841–852.

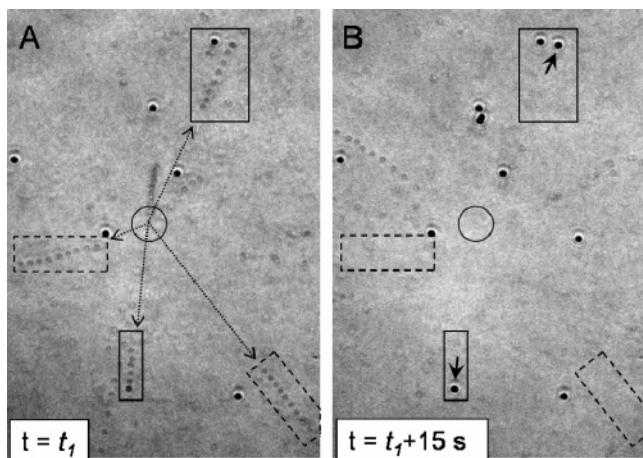


Figure 5. Transport and deposition of low velocity CML particles onto alginate conditioning film at an ionic strength of 30 mM (KCl) in the RSPF system. Deposition is detected by comparing two successive pictures of the surface (A, at time = t_1 , and B, at time = $t_1 + 15$ s). By superposing nine successive pictures taken over a total time of ~ 3 s, low velocity particles in the vicinity of the substrate appear as a succession of 9 aligned points. Particles are swept away by the radial flow from the center (circle) toward the outside boundary of the stagnation point (dashed arrows). Among the particles of low velocity, some particles can deposit (traced in solid frames, with the newly adhering particle shown with solid arrow) and others do not (traced in dashed frames). The capillary flow rate in the RSPF system was fixed at 4.93 mL/min (average velocity of 26.5 cm/s), resulting in a capillary Reynolds number of 28.4 and a particle Peclet number of 0.22. Other experimental conditions employed were an ambient pH (5.5–5.7) and a temperature of 25 °C (± 1 °C).

were depicted by the appearance on two successive pictures of a dark particle at the end of the trajectory of nine aligned points. We showed that, among the particles trapped in a secondary energy minimum and entrained by the radial flow (Figure 5A), a significant portion of them irreversibly deposited (Figure 5B). Direct evidence of this irreversible deposition from secondary minimum entrapment was only recorded during particle deposition onto alginate films at ionic strengths between 30 and 300 mM. The lack of observation of this phenomenon onto bare quartz under similar or lower ionic strength conditions suggests that the conditioning film is crucial for the irreversible attachment of particles trapped in secondary minima.

This novel experimental evidence of particle deposition from secondary minimum entrapment in RSPF systems points to the importance of incorporating this deposition mode into interpretations and predictions of deposition kinetics. The irreversible deposition of trapped particles is likely to be favored by surface properties of the conditioning film such as enhanced roughness²¹

and local charge/chemical heterogeneities.⁴⁷ Surface asperities have been shown to cause significant reduction in the average repulsive interaction energy between particle and substrate, the extent of which depends on the size of the asperities and their densities on the conditioned surface.⁴⁸ Local charge heterogeneities can be formed due to the weak acidity of our system. Alginate polysaccharides have a pK_a between 3.5 and 4 and are likely to be partially uncharged at ambient pH (pH 5.5–5.7). These charge heterogeneities of the film that induce attractive interactions with the particle could form localized reduction of the total repulsive interaction energy. Consequently, particles trapped in secondary minima wells could transit more easily between the secondary energy well and the primary minimum.¹³

3.5.2. Bacterial Cells. Because of optical limitations of the RSPF setup when imaging bacteria, we were unable to collect clear images, as those shown in Figure 5, that could demonstrate the irreversible deposition of bacteria that were trapped in the secondary minimum. Nonetheless, the occurrence of this phenomenon was also observed during the bacterial deposition experiments (data not shown), indicating that this mode of deposition is not exclusive to CML particles. Assuming that the irreversible attachment is affected by the heterogeneities of the polymeric structures on the surface, we can predict that the larger heterogeneities of cell surface appendages (compared to CML particles) favor the deposition of bacteria that are trapped in secondary minima. Therefore, the deposition of bacterial cells from secondary minimum entrapment could explain, in part, the discrepancy between the slopes of our experimental and theoretical deposition kinetics.

4. Conclusion

Deposition kinetics of bacteria onto an alginate conditioning film were compared to DLVO predictions of cell deposition. The marked discrepancies between experiments and theory were discussed in terms of the presence of structural and physico-chemical heterogeneities at the cell and substrate surfaces. Microscopic analysis provided evidence for the irreversible deposition of particles (and cells) that were trapped in the secondary energy minimum. This mode of deposition is proposed to be one of the main causes for the substantial underestimation of deposition kinetics predicted by the DLVO theory.

Acknowledgment. The work was supported by the Water-CAMPWS, a Science and Technology Center of Advanced Materials for the Purification of Water with Systems under the National Science Foundation agreement, Number CTS-0120978.

LA701936X

(47) Xu, L. C.; Logan, B. E. *Langmuir* **2006**, *22* (10), 4720–4727.

(48) Bhattacharjee, S.; Ko, C. H.; Elimelech, M. *Langmuir* **1998**, *14* (12), 3365–3375.